

# Inhibiting Nonradiative Recombination and Scattering Losses via Ultrafast Pulse Irradiation for Enhanced Perovskite Lasing

Rahul A. Rajan, Xiaobao Ma, Dabing Li, Zhiming Shi,\* Weili Yu,\* and Jianjun Yang\*

Cite This: *ACS Photonics* 2023, 10, 3255–3265

Read Online

ACCESS |



Metrics &amp; More



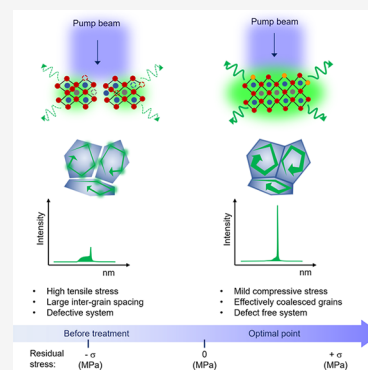
Article Recommendations



Supporting Information

**ABSTRACT:** Lasing performance of solution-processed perovskite thin films is strictly limited by the out-of-plane scattering losses due to the wide intergrain spacings and quick nonradiative recombination at grain boundaries. Here, we show a novel strategy to regulate the morphology and properties of perovskite films with the femtosecond laser treatment, which effectively coalesces the adjacent grain boundaries and tunes the deep defect density. The experimental results along with the density functional theory calculations demonstrate that the mild residual compressive stress condition ( $0 \text{ MPa} < \sigma < -15 \text{ MPa}$ ) originating from the ultrafast nonthermal modification helps to increase the defect formation energy, thus reducing the density of deep defects, and prolongs the excited carrier lifetime for the suitable population inversion. As a result, the random lasing threshold of the perovskite thin films is dramatically reduced to a record value of  $0.92 \mu\text{J}/\text{cm}^2$ , with a 15-fold improvement in the output slope efficiency. This research will stimulate more investigations on developing high-performance perovskite light sources by the precise tuning of crystalline properties with ultrafast pulses.

**KEYWORDS:** femtosecond laser treatment, perovskite thin films, grain boundary coalescence, strain modulation, defect engineering, random lasing



## INTRODUCTION

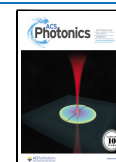
The development of high-performance micro- and nanoscale laser sources has always been a central subject among the semiconductor laser research community, because of their valuable potential in optoelectronics and high-resolution imaging.<sup>1–11</sup> As an excellent emerging candidate for solution-processable lasers, perovskite materials including nanostructures, single crystals, and thin films have recently attracted wide attention,<sup>12–19</sup> due to their well-known peculiar characteristics such as high absorption coefficient, long carrier lifetime, facile solution processability, and broad wavelength tunability in the whole visible spectrum.<sup>20–22</sup> During the past few years, some significant progress based on perovskite thin films has been reported in variable applications, including highly efficient solar cells,<sup>23</sup> multicolor light emitting diodes,<sup>1,24,25</sup> and high-performance optically pumped lasers.<sup>26,27</sup> By using the spin-coated perovskite thin films, the random lasing (RL) can be simply realized with the feedback process from multiple scatterings of the naturally disordered structures such as grain boundaries and phase transitions.<sup>28–30</sup>

Noticeably, some significant efforts have also been made to enhance the optical gain and RL behaviors of the perovskite thin films, which are mostly concentrated on the modification of the substrate with different techniques, including hydrophobic functionalization,<sup>31</sup> surface patterning,<sup>32</sup> and increasing the localized curvature of flexible substrates.<sup>33</sup> Accordingly, the random light scattering can be intensified to decrease the RL

threshold to a few  $\text{mJ}/\text{cm}^2$  levels. Furthermore, by adjusting the parameters of the perovskite thin films such as the grain size and nanocrystal occupancy, the previous studies have demonstrated the control of the laser peak wavelength and the reduction of the lasing threshold to hundreds of  $\mu\text{J}/\text{cm}^2$ .<sup>34,35</sup> Recently, Shi et al. observed the amplified spontaneous emission (ASE) with a low threshold of  $5.6 \mu\text{J}/\text{cm}^2$  after the secondary crystallization of inorganic perovskite  $\text{CsPbBr}_3$  NC films through the nanosecond laser treatment, where the laser-induced thermal effect is mainly responsible for improving the crystalline quality and reducing the nonradiative recombination pathways. However, considering the degradation of organic elements under thermal effects, the viability of such techniques associated with superior thermal effects is questionable for a large number of bulk organic–inorganic perovskite thin films. On the other hand, to achieve superior performance with the perovskite RLs, the perovskite thin films should essentially possess high crystalline quality, compact grain arrangements, and low defect density. Whereas when the  $\text{MAPbBr}_3$  thin film is spin-coated on the glass substrate, the

Received: May 20, 2023

Published: September 9, 2023



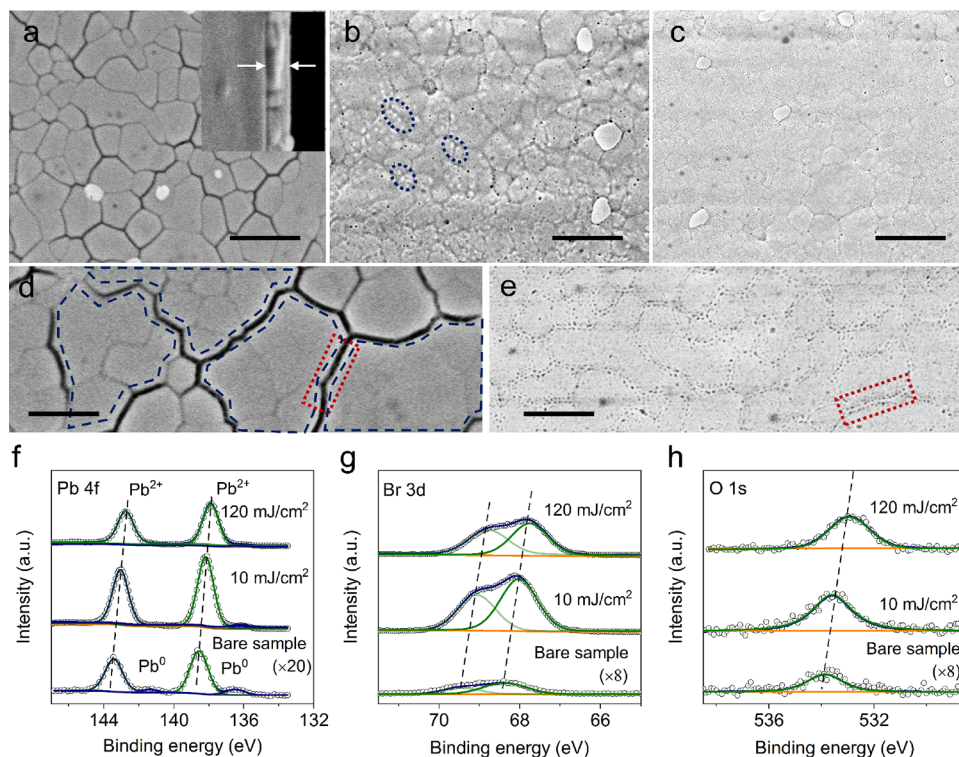


**Figure 1.** Morphology and chemical variations of the MAPbBr<sub>3</sub> thin film before and after the femtosecond laser treatments. (a) Bare sample, in which the inset picture gives the film thickness around 170 nm. (b, c) Surface morphologies of the thin films after the laser treatment with different energy fluences of  $F_{\text{treat}} = 10$  and  $120 \text{ mJ/cm}^2$ , respectively. Scale bar:  $1 \mu\text{m}$ . (d, e) Magnified SEM images for the surface morphology of the bare and femtosecond laser-treated sample (with  $F_{\text{treat}} = 120 \text{ mJ/cm}^2$ ), respectively, where the bare sample consists of islands of grain clusters with a wide gap  $\sim 20 \text{ nm}$ , and after the laser treatment, the adjacent grains seem to coalesce together as highlighted with a brown dotted rectangle. Scale bar:  $300 \text{ nm}$ . (f–h) XPS spectra of Pb 4f, Br 3d, and O 1s for the bare and laser-treated MAPbBr<sub>3</sub> surface. The data of the bare sample in panels f–h are scaled up by 20, 8, and 8 times, respectively.

thermal expansion mismatch between these two materials makes the perovskite grains restricted from contracting while cooling back to room temperature. Inevitably, a substantial tensile strain can be developed in the thin film along the in-plane direction, resulting in various deep defects from the misfit dislocation<sup>36</sup> and wide intergrain spacings/cracks of the perovskite materials. In general, because of the strong adhesion between the thin film and substrate, such residual tensile strain in the perovskite films is hard to change via conventional postprocessing methods. Consequently, the current status of the solution-processed perovskite thin-film samples still encounters two major problems that prevent their usage for high-performance laser devices. One is the out-of-plane scattering losses and weak light confinement due to the existence of wide intergrain gaps. The other is the quick nonradiative recombination centers because of the deep defect density along the grain boundaries,<sup>37</sup> which prohibits further lowering of the RL threshold.

Herein, we propose a novel strategy to manipulate the crystalline properties of the organic–inorganic perovskite thin films by regulating the strength of the femtosecond laser-induced nonthermal and thermal effects, which consequently leads to an effective grain boundary coalescence and decreases in the nonradiative deep defect density along the grain boundaries. The experimental results along with the density functional theory (DFT) calculations unveil that the induced nonthermal effect like the mild compressive stress can increase the formation energy of various defects, thereby effectively reducing the deep defect density, which is evidenced by the

prolonged photoluminescence (PL) lifetime and enhanced PL intensity. Subsequently, we observed the RL emission with no sharp spikes present in the emission spectra, which indicates that it belongs to the incoherent RL emission with a nonresonant/incoherent feedback.<sup>28</sup> Eventually, through this ultrafast nonthermal manipulation method, we can greatly lower the RL threshold value from  $11.54$  to  $0.92 \mu\text{J/cm}^2$ .

## RESULTS AND DISCUSSION

**Spatial Coalescence of Grain Boundaries by Femtosecond Laser Treatment.** We attempt to modify the crystalline properties of MAPbBr<sub>3</sub> thin films on glass substrates by regulating the nonthermal and thermal effects of the femtosecond laser treatment. The femtosecond laser has the central wavelength of  $\lambda_{\text{treat}} = 800 \text{ nm}$  and the pulse duration of  $\tau = 40 \text{ fs}$ , associated with variable energy fluences of  $F_{\text{treat}} = 10, 20, 40, 80,$  and  $120 \text{ mJ/cm}^2$ , respectively (see supplementary section 1 for the detailed information about the experiments). Figure S1 shows a schematic of the optical setup for the femtosecond laser treatment. As the absorption onset of MAPbBr<sub>3</sub> perovskite materials occurs at around the wavelength of  $532 \text{ nm}$  (Figure S2) with an absorption coefficient of  $10^5 \text{ cm}^{-1}$ , the femtosecond laser excitation is physically based on a two-photon process.

The surface morphologies of thin-film MAPbBr<sub>3</sub> before and after the laser treatments are analyzed by scanning electron microscopy (SEM). Figure 1a shows an as-prepared MAPbBr<sub>3</sub> sample with a thickness of around  $170 \text{ nm}$ . Figure 1b,c illustrates the surface morphologies of the perovskite samples

treated by the femtosecond laser pulses with energy fluences of  $F_{\text{treat}} = 10$  and  $120 \text{ mJ/cm}^2$ , respectively. After the laser treatment, we found that the sample surface at  $F_{\text{treat}} = 10 \text{ mJ/cm}^2$  contains abundant nanobumps along the grain boundary edges (marked with the dotted circles). Also, under the fluence of  $F_{\text{treat}} = 10 \text{ mJ/cm}^2$ , the grain may come closer and even coalesce, leading to reduced intergranular spacing. Notably, when increasing the energy fluence of the laser treatment, the sample surfaces become smooth, but with appearing pinholes along the grain boundaries (Figure S3). Our results show that the wide intergrain gaps present in the perovskite thin film can be modified by changing the laser treatment fluence (as highlighted in Figure 1d,e).

We then tried to figure out how the femtosecond laser treatment affects or coalesces the adjacent grains with the minimum pinholes in the film. The elaborate modification process is believed to be related to the magnitudes of the femtosecond laser-induced nonthermal and thermal effects.<sup>38</sup> For the nonthermal effect, it is known that the lattice arrangement in a crystalline material is intricately connected with the state of the electrons in the material.<sup>39</sup> This means that the valence electrons in the semiconductor determine the most energetically stable arrangement of the ionic core of the atoms. When roughly 10% of the bonding electrons is excited to the antibonding orbitals by the femtosecond laser irradiation, free carrier plasma is produced, and thus, the potential energy distribution around the ions is modified to consequently influence the lattice arrangement. In other words, under such circumstances, the photo-excitation of electrons itself can give the atoms enhanced mobility to reorganize the lattice system and modulate the residual stress, which is the so-called nonthermal plasma model in many previous reports.<sup>38–40</sup>

In another perspective, the nonthermal effect is explained by the hot-electron blast model; according to that, a sudden blast force of hot-electron on cold lattice can also deform the lattice structures upon the femtosecond laser irradiation.<sup>41</sup> That means, due to the stark difference in the specific heat capacities of the electron and lattice ( $C_e < C_l$ ), the incident femtosecond laser pulse raises the temperature of the electrons much higher than the lattice within the optical penetration depth while the lattice remains thermally cold. Falkovsky and Mishchenko comprehensively presented that the material lattice can be effectively deformed by making use of a driving force known as the hot-electron blast force, which is brought on by the nonequilibrium electron state under ultrashort laser irradiation.<sup>41</sup> This force is proportional to the gradient of electron temperature squared ( $\nabla T_e^2$ ).<sup>41,42</sup> When the electron temperature increases drastically, the hot-electron blast force becomes sufficient enough to modify the crystal lattice arrangement before achieving electron-lattice equilibrium. It shows that the femtosecond laser treatment can effectively modulate the residual stress without any vibrational energy that arises from the thermal effect. This way of structural change is known as the laser-induced nonthermal modifications.<sup>38,42–44</sup>

In addition to the nonthermal effect, the femtosecond laser irradiation can also cause thermal effects or melting after the electron–phonon equilibration. This can be understood as follows: due to the high defect density, the thermal conductivity along the perovskite grain boundaries is significantly lower than that inside the grains.<sup>45</sup> Therefore, after the ultrashort pulse irradiation, the high temperature is

considerably raised near the grain boundaries via the phonon–phonon and phonon-defect scatterings,<sup>38</sup> which leads to the melting of the grain boundaries along with the adiabatic expansion.<sup>38,46</sup> In this research, such a rapid thermal expansion coalesces the grain boundaries together to eliminate the wide intergrain gaps. During this process, the higher specific volume of the molten material adds compression to the surroundings. Such compressive stress (a kind of thermo-elastic stress due to the temperature gradient) also modifies the crystal lattice arrangement for reducing the amplitude of the residual in-plane tensile stress in the perovskite film. However, while the perovskite grains contract back to their original condition, an unloading tensile component of the induced compressive stress is created. Such tensile stress can induce cavitation and nanoscale pinholes in the molten part of the grains along the grain boundaries. Although such pinhole formation can help to release the unloading tensile component of the laser-induced stress, they are detrimental to the stability of the perovskite thin films. Thus, the formation of such pinholes through the thermo-elastic or thermal effects should be minimized. A detailed analysis of surface morphology for both the bare and laser-treated perovskite films (Figure S3 and Figure 1e) shows that the pinhole formation due to the thermal effect or the thermo-elastic stress is more pronounced at higher laser fluences ( $F_{\text{treat}} > 20 \text{ mJ/cm}^2$ ) and becomes less at lower laser fluences ( $F_{\text{treat}} \leq 20 \text{ mJ/cm}^2$ ). Hence, for the better performance of the perovskite thin film, the latter condition of the laser treatment is more suitable than the former.

We then performed X-ray photoelectron spectroscopy (XPS) to evaluate the chemical composition change for the perovskite thin-film surface before and after the coalescence of grain boundaries. It was observed that, by increasing the laser treatment energy fluence from  $F_{\text{treat}} = 10$  to  $120 \text{ mJ/cm}^2$ , the available peaks of Pb 4f (at 143.4 and 138.5 eV), Br 3d (at 69.4 and 68.3 eV), and O 1s (at 533.9 eV) are slightly shifted to the lower binding energy positions (see Figure 1f–h). The peak intensities of Pb 4f and Br 3d also tend to increase after the laser treatment, whose increment seems to be pronounced at  $F_{\text{treat}} = 10 \text{ mJ/cm}^2$  in comparison with  $F_{\text{treat}} = 120 \text{ mJ/cm}^2$ . This might be due to the formation of nanobumps along the grain edges in the former case, which tends to increase the surface areas and facilitate the reaction between the film and atmospheric oxygen. That is also confirmed by the increased intensity and peak shift of Pb 4f and O 1s, which shows the chemical reaction between lead and atmospheric oxygen that leads to the formation of the Pb–O bonds.<sup>47</sup> Along with this happening, the laser-induced adjacent grain coalescing effect can subsequently reduce the presence of  $\text{Pb}^0$  accompanied by the lower energy shift and broadening of the  $\text{Pb}^{2+}$  peak (at 138.5 eV). The observed peak broadening is typical for metal oxide components, and it shows that the  $\text{Pb}^0$  components are oxidized to  $\text{Pb}^{2+}$ .<sup>47</sup> These findings clearly demonstrate a conversion from  $\text{Pb}^0$  to Pb–O, or heavy oxidative passivation, during the coalescence of grain boundaries in the ambient environment. After all, the measured higher intensities of Pb 4f and O 1s peaks in the case of  $F_{\text{treat}} = 10 \text{ mJ/cm}^2$  indicate the maximum Pb–O reaction taking place at this sample surface. According to recent studies, during this process, the non-radiative recombination centers along the grain boundaries will undergo oxygen-induced defect passivation.<sup>48,49</sup> That means, when the femtosecond laser beam strikes the sample in air, the reactive oxygen species assist to passivate the halide vacancies like V(Br) and cure the nonradiative charge recombination



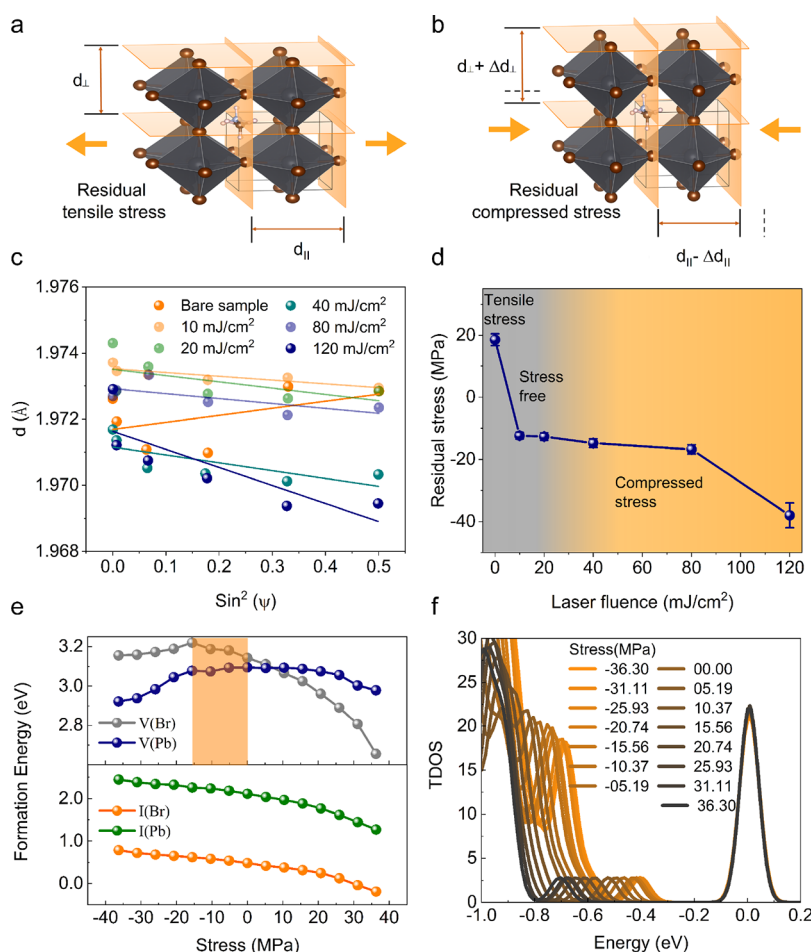


**Figure 2.** Residual stress and nature of the defects in perovskite thin films before and after the laser treatments. (a, b) Physical diagrams for the perovskite crystals consisting of the residual tensile stress and compressive stress before and after the laser treatment, respectively, in which arrows at the left- and right-hand sides of the crystal structure indicate the direction of the induced residual stress. (c) Illustration of the residual stress in a plot obtained by the  $d \sim \sin^2(\psi)$  method. (d) The measured variations of the residual stress in the bare and laser-treated perovskite samples. (e) The calculated formation energy of defects and (f) TDOS of the I(Br) as a function of the stress in the MAPbBr<sub>3</sub> crystalline structure.

centers.<sup>50</sup> This process will lead to the photo-brightening effect, which increases the PL yield of the perovskite materials.<sup>48,50</sup>

To further understand the variation of defect density induced by the irradiation of the femtosecond laser pulses, it is important to examine the modulation of crystalline properties as a function of the laser treatment parameters.<sup>38,46</sup>

**Reduction of the Defect Density by the Laser-Induced Nonthermal Effect.** We then examined the tuning of residual stress by the femtosecond laser irradiation, which may modify the crystalline properties of the perovskite thin film and affects the defect formation energy ( $E_{\text{form}}$ ) and inhibits the overall deep defect density ( $n_x$ ). To comprehensively understand the crystalline property change, we employed the grazing incidence XRD (GIXRD) and micro-XRD ( $\mu$ XRD) methods and analyzed the nonuniform residual strain in the samples along the in-plane and out-of-plane directions, respectively (see supplementary section 3 for the detailed information).

During the spin coating process, a considerable residual tensile strain is generated in the prepared thin film along the in-plane direction (Figure 2a). The presence of such residual tensile stress, mainly in the in-plane direction is confirmed through the  $d \sim \sin^2(\psi)$  mode of XRD measurements, which

directly probe the total residual stress by measuring the interatomic spacing of the perovskite crystal lattice (Figure 2c).<sup>51,52</sup> As shown in Figure 2b and Figure S7b, the perovskite crystals experience in-plane compression and out-of-plane expansion upon the femtosecond laser treatment. Figure 2d shows that the in-plane residual tensile stress inside the MAPbBr<sub>3</sub> thin film is gradually transformed into the in-plane compressive stress with increasing laser treatment fluences. When the laser treatment fluence is  $F_{\text{treat}} = 10$  mJ/cm<sup>2</sup>, not only the tensile stress of  $\sigma = 18.6 \pm 1.9$  MPa in the bare sample is completely relaxed, but also the additional mild compressive stress of  $\sigma = -12.4 \pm 1.1$  MPa is newly introduced. It confirms that the laser-induced stress is compressive in nature; thus, it can effectively nullify the residual tensile stress present inside the thin film and induce additional compressive stress. In addition, to understand the laser-induced compression in the in-plane and out-of-plane directions, both the residual microstrain and interplanar distance of the {100} planes in the MAPbBr<sub>3</sub> film were also measured (Figure S7). These results also confirm that the magnitude of the residual in-plane tensile strain ( $\epsilon_{\parallel}$ ) and interplanar distance in the in-plane direction ( $d_{\parallel}$ ) are continuously reduced after the laser treatment. Such residual stress relaxation along with the maximum oxygen-induced defect passivation (discussed in the

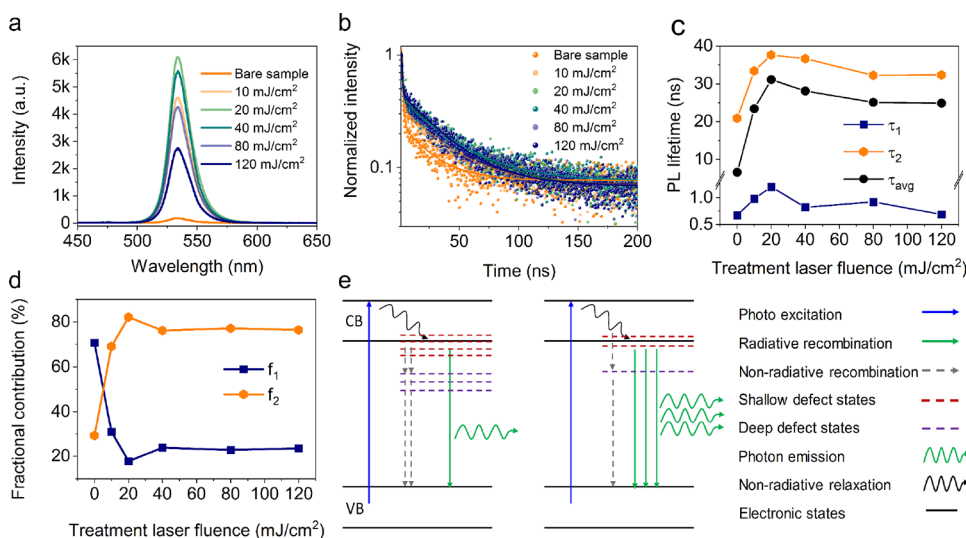


**Figure 3.** Optical characterizations of the thin-film perovskite samples before and after the femtosecond laser treatment. (a) Static PL spectra and (b) time-resolved PL spectra with biexponential decay-fitted curves associated with the bare and laser-treated samples. (c) The measured lifetimes of average PL and two decaying pathways ( $\tau_1$  and  $\tau_2$ ), and (d) fractional contributions of the two decaying processes ( $f_1$  and  $f_2$ ) before and after the laser treatment. (e) An illustration of the energy level diagram and most probable recombination mechanisms of the perovskite sample before (left) and after (right) the laser treatment. CB and VB represent the conduction band and valence band, respectively.

previous section) can offer improved crystallinity for the samples treated at  $F_{\text{treat}} = 10 \text{ mJ/cm}^2$ ; this is confirmed through the analyses of GIXRD peaks (Figure S8). With the higher energy fluence of  $F_{\text{treat}} = 120 \text{ mJ/cm}^2$ , the laser introduced compressive stress is further increased to  $\sigma = -38.0 \pm 4 \text{ MPa}$ .

We then examined the defect chemistry modification of the MAPbBr<sub>3</sub> crystalline structure through the DFT calculations under the similar stress conditions. Here, four types of defects are considered, including Pb/Br vacancies V(Pb/Br) and interstitial I(Pb/Br). As for MA defects, we projected the band edge wave function into the real space (Figure S9a,b) and found no contribution of the MA molecule to the band edge. As shown in Figure S10, by comparing with the pure MAPbBr<sub>3</sub>, the most stable structures with I(Pb) and I(Br) appear to be endured at intrinsic tensile stress conditions (positive values). It can be ascribed to the volumetric expansion induced by the interstitial atoms. To investigate the stress effect on the formation of defects, we calculated the formation energy of defects under different stress conditions (see Figure 2e).

The relationship between the  $n_x$  and formation energy can be described by the Arrhenius equation:

$$n_x = n_0 e^{-E_{\text{form}}/k_B T} \quad (1)$$

where  $n_0$ ,  $E_{\text{form}}$ , and  $k_B$  represent the areal atom density, the formation energy of the defect, and Boltzmann constant, respectively. It shows that, at a certain temperature, the  $n_x$  value decreases with a larger  $E_{\text{form}}$ . According to the calculation results, the calculations of I(Br) show the lowest  $E_{\text{form}}$  among the four defects by at least 1 eV, and it even becomes negative while increasing the tensile stress by more than 30 MPa, which implies the highest defect density at the tensile stress conditions. Furthermore, as shown in Figure 2e, the calculated  $E_{\text{form}}$  for interstitial defects appears to monotonously increase with the larger compression, and thus, the density of the interstitial defects will be reduced by applying the compressive stress condition to the materials. These results indicate that, when compressive stress is applied, the distance between the

atoms will be decreased to result in enhancing the Coulomb interactions. In addition, the volume of the crystal was also reduced, so that there is the less space inside the crystal to accommodate interstitial impurity atoms, which leads to the increase of  $E_{\text{form}}$  for the associated defects. On the other hand,  $E_{\text{form}}$  values for V(Br) and V(Pb) reach the maximum at  $\sigma \approx -15$  and 0 MPa, respectively, and gradually reduce when further increasing either compressive or tensile stress conditions. This is the result of the competition between the intrinsic and dangling bonds to achieve stability. In MAPbBr<sub>3</sub>, the Br vacancies act as the major nonradiative recombination centers; thus here, we adopt the V(Br) as an example. Its  $E_{\text{form}}$  values gradually increase due to the dangling bond stabilization, while the compressive stress increases from 0 to -15 MPa. However, when further increasing the compressive stress condition, the free energy rises in the system due to the intrinsic bonds suffering from serious instability. As a consequence, higher compressive stress conditions can introduce higher  $n_x$  of V(Br) and V(Pb), which are the major nonradiative recombination centers in MAPbBr<sub>3</sub> perovskite films. These results suggest that a mild compressive stress condition ( $0 \text{ MPa} < \sigma < -15 \text{ MPa}$ ) should be maintained to achieve the lowest  $n_x$  (highlighted in Figure 2e). Noticeably, the lower laser treatment fluence of  $F_{\text{treat}} \leq 20 \text{ mJ/cm}^2$  can induce similar residual compressive stress condition (Figure 2d), which might be predominantly from the nonthermal effect (as discussed in the previous section).

As I(Br) defects are easily generated due to their relatively lower formation energy than the other defects, it is important to look at its defect state formation in the energy band gap. The calculated total density of states (TDOS) of I(Br) is shown in Figure 2f. It is observed that the defect states for I(Br) became more shallow (i.e., close to VBM) with increasing compression, which is because the induced compressive stress could change the location of the band edge.<sup>53</sup> This can largely reduce the I(Br) defect-mediated nonradiative (Shockley-Read-Hall, SRH) recombination because the trapped carriers in shallow defect states have a high

probability of detrapping.<sup>54</sup> The results demonstrated that, by applying the stress conditions of  $0 \text{ MPa} < \sigma < -15 \text{ MPa}$  through the optimum laser-induced nonthermal effect ( $F_{\text{treat}} \leq 20 \text{ mJ/cm}^2$ ), the  $E_{\text{form}}$  can effectively increase to inhibit the overall  $n_x$  and push the defect states more close to the band edges. Hence, it might be beneficial to enhance the luminescence behavior of MAPbBr<sub>3</sub> thin films. The following section investigates the optical properties of the bare and laser-treated samples based on the static PL and TRPL measurements.

**Optical Properties of Femtosecond Laser-Treated MAPbBr<sub>3</sub> Thin Films.** To deeply understand the excited carrier recombination mechanisms, we carried out the static and time-resolved PL measurements. Figure 3a and Figure S11 show the measured room-temperature PL emission spectra for different MAPbBr<sub>3</sub> perovskite films. Compared with the bare sample, the PL emission intensity of the laser-treated perovskite film is enhanced about 31 times for the case of  $F_{\text{treat}} = 20 \text{ mJ/cm}^2$ . This higher PL enhancement can be attributed to the laser-induced deep defect passivation along the grain boundaries and subsequent photo-brightening effect as observed from the XPS measurement results. We investigated the bandgap modulation of the samples with the UV–vis absorption spectra and Tauc analysis (see supplementary section 2). The results show that the bandgap energy of  $E_g = 2.310 \text{ eV}$  associated with the bare sample is narrowed to  $E_g = 2.302 \text{ eV}$  (a reduction of  $E_g = 8.0 \text{ meV}$ ) when increasing laser treatment fluence to  $F_{\text{treat}} = 80 \text{ mJ/cm}^2$ . It shows that excessive femtosecond laser-induced compression might introduce some trap states by affecting the crystalline nature of MAPbBr<sub>3</sub>,<sup>55</sup> which suggest to optimize the laser treatment energy around 10 and 20  $\text{mJ/cm}^2$  for better optoelectronic performance.

The recombination dynamics of photoexcited carriers was investigated by TRPL spectroscopy, and then, it is represented by the following rate equation

$$\frac{dn}{dt} = -An - Bn^2 - Cn^3 \quad (2)$$

where  $n$  is the excited carrier density,  $t$  is the time, and  $A$ ,  $B$ , and  $C$  are the rate coefficients that represent the mono-molecular trap-assisted recombination, bimolecular radiative recombination, and three-body Auger recombination, respectively.<sup>56</sup> Generally, in bulk perovskites, the trap-assisted nonradiative recombination plays a dominant role over Auger recombination because the less spatial confinement decreases the overlap of charge carrier wavefunctions.<sup>57</sup> The PL decaying traces of the samples were notably different from each other (see Figure 3b). Each curve was fitted with a biexponential decay function of  $I(t) = A_1 \exp(-t/\tau_1) + A_2 \exp(-t/\tau_2)$  to analyze the PL lifetime components and understand the carrier recombination dynamics, which comprises a short lifetime ( $\tau_1$ , hundreds of ps), long lifetime ( $\tau_2$ , tens of ns), and corresponding fractional contributions  $f_1$  and  $f_2$  of the deep and shallow trap state recombinations, respectively.<sup>58,59</sup> The detailed measurements of  $\tau$  and  $f$  are included in supplementary Table S2. The average PL lifetime of the bare MAPbBr<sub>3</sub> sample ( $\tau_{\text{avg}} = 6.60 \text{ ns}$ ) is similar to that reported by the previous literatures.<sup>60,61</sup> After the laser treatment,  $\tau_{\text{avg}}$  showed a maximal enhancement in the case of  $F_{\text{treat}} = 20 \text{ mJ/cm}^2$ , which is about 371.35% longer than the bare sample.

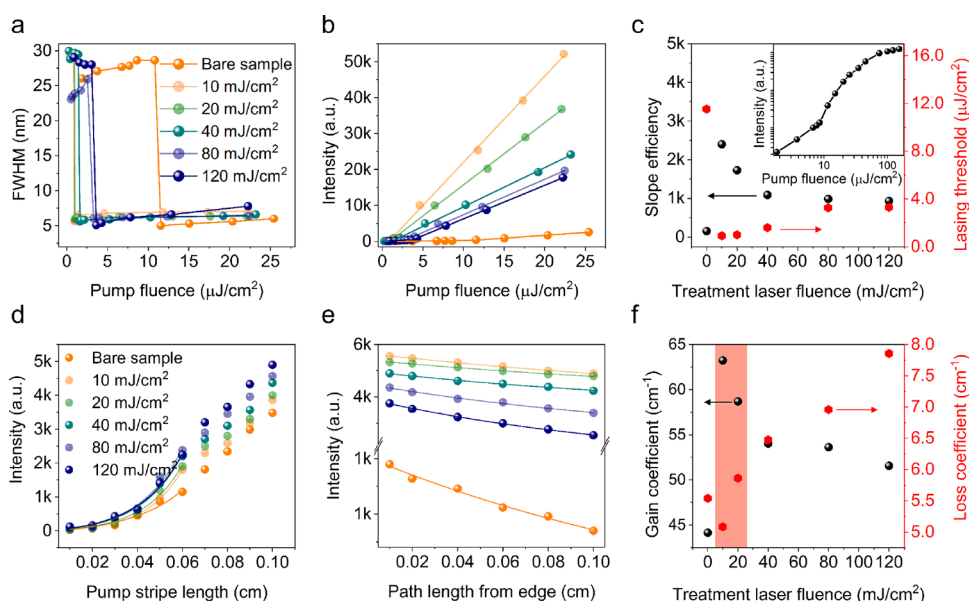
The dependences of the excited carrier lifetime components ( $\tau_1$  and  $\tau_2$ ) on the femtosecond laser fluence are shown in Figure 3c, wherein both  $\tau_1$  and  $\tau_2$  show a similar variation trend as that of  $\tau_{\text{avg}}$  with different laser treatment fluences. The observed enhancement of the  $\tau_1$  value for the laser-treated sample at the energy fluences of  $F_{\text{treat}} = 10$  and  $20 \text{ mJ/cm}^2$  can be understood by the structural crystallinity improvement from the grain boundary coalescence that consequently reduces the number of quick deep trap states and increases the bimolecular recombination.<sup>56</sup> Also, the increment of the  $\tau_2$  value for the perovskite samples treated with the laser fluences of  $F_{\text{treat}} = 10$  and  $20 \text{ mJ/cm}^2$  was mainly based on the recombination of free excitons and the localized/bound excitons trapped at shallow trap states,<sup>62,63</sup> providing the PL lifetime in a range of tens of nanosecond. It is worth mentioning that, as the trapped carriers in shallow trap states generally have the high probability of detrapping, it is not detrimental for achieving necessary population inversion conditions to realize an efficient laser. The DFT calculation results show that, under the situation of intense compressive stress, the formation energy of V(Pb/Br) slightly decreases (see Figure 2e). Hence, the laser treatments with the energy fluences of  $F_{\text{treat}} \geq 40 \text{ mJ/cm}^2$  might easily create more V(Pb/Br) to introduce new deep defect states (mostly nonradiative recombination centers) inside the sample,<sup>64</sup> which can slightly decrease  $\tau_{\text{avg}}$ ,  $\tau_1$ , and  $\tau_2$  as depicted in the graph (Figure 3c).

Figure 3d illustrates the measured variations of both  $f_1$  and  $f_2$  (corresponding to the deep and shallow regions, respectively) with different laser treatment fluences. In the case of PL from a bare sample,  $f_1$  initially dominates  $f_2$ , but after the femtosecond laser treatment, the contribution flipped dramatically. The variation trend of  $f_1$  and  $f_2$  demonstrates that, upon the femtosecond laser treatment, the free excitons and bound excitons with the shallow states cause more radiative recombinations and which is maximum at  $F_{\text{treat}} \leq 20 \text{ mJ/cm}^2$ . When the laser treatment fluence is  $F_{\text{treat}} \geq 40 \text{ mJ/cm}^2$ , the excessive compressive strain would like to create more V(Pb/Br) and crystalline deformation to result in more nonradiative recombination centers. These measurement results indicate that the femtosecond laser treatment with the optimum fluence (i.e.,  $F_{\text{treat}} \leq 20 \text{ mJ/cm}^2$ ) is an effective method to greatly increase the carrier lifetime in the perovskite samples, thus suitable to prepare the sample for a low threshold laser device.

Based on these observations, we illustrate the carrier recombination mechanisms for the bare and laser-treated perovskite samples, as shown in Figure 3e. To achieve the optical gain through light amplification, the excited carriers must be populated in the conduction band (CB). This physical process is usually interrupted by various nonradiative pathways. As per eq 2, the trap-assisted recombination is one of two major nonradiative pathways that must be suppressed. Especially, the trap-assisted recombination through deep defects such as vacancies can rapidly deplete the carrier population from the CB within the femtosecond-to-picosecond time scales.<sup>65,66</sup> As shown in previous sections, the mild compressive condition and oxygen-assisted grain boundary coalescence are apt to reduce the nonradiative deep defect density. Eventually, this enables the perovskite sample to achieve the population inversion under the proper laser pumping conditions, resulting in the efficient optical amplification.

**Improvement of RL Performance.** We then explored the room-temperature RL characteristics of the laser-treated





**Figure 4.** Measured RL, optical gain, and loss coefficient from the perovskite samples before and after the femtosecond laser treatment. (a) Observation of the narrowing effect in the output spectra and (b) the measured variation of the emission intensity of all samples as a function of the pump fluence (represented with the dots), along with the fitting (represented by the lines) and (c) the variations of the slope efficiency and lasing threshold in terms of the laser treatment fluence, in which the inset picture shows the pump fluence versus the emission intensity on a log-log scale. (d) The measured gain coefficient of all the samples through the variable stripe-length method and (e) the calculated optical loss coefficient of the samples by measuring the edge emitting intensity as a function of the excitation distance from the edge. The measured data are represented by the dots, and fitting is represented by the lines. (f) Modulation of the gain and loss coefficients with respect to the laser treatment fluence.

MAPbBr<sub>3</sub> perovskite thin films. In the regular laser design, the continuous oscillations between the spatially separated reflectors give rise to a certain lasing mode generation and sufficient optical gain. Whereas in our case, the large-spot optical pumping with a central laser wavelength of  $\lambda_{\text{pump}} = 400$  nm can generate multiple in-plane optical loops within the film due to the in-plane scattering from the grain boundaries and various structural disorders.<sup>30</sup> Therefore, the multiple light scatterings within the disordered MAPbBr<sub>3</sub> sample confine the photons inside for adequate time to provide sufficient amplification. Upon the light pumping, the photons are generated by the recombination of bound excitons and then undergo further amplification by the stimulated emission. The measurements of pump energy-dependent RL spectra for the bare MAPbBr<sub>3</sub> thin films are shown in Figure S12a, where a single peak of spectrum is observed with only a few nanometers in the full-width-at-half-maximum (FWHM). This single-peak observation can be considered as a result of multiple scatterings from the grains of various dimensions within the large pumping area, which is averaged over a number of pumping laser shots, along with the long effective mean free path length (longer than the emission wavelength) of the diffusive light propagation.<sup>29</sup>

As shown in Figure S12b, for the pump fluences lower than the lasing threshold ( $F_{\text{pump}} = 11.54 \mu\text{J}/\text{cm}^2$ ), a broad emission spectrum was obtained at the wavelength of about 533 nm with around 28 nm in FWHM. When the pump fluence reached the threshold value, a distinguishable lasing spectrum was developed at the wavelength of  $\lambda_{\text{lasing}} = 549$  nm, with the accompaniment of the drastically reducing linewidth to  $\sim 3.0$  nm. The lasing spectral intensity tends to rapidly increase for the pump light fluence higher than the lasing threshold, at which the variation of emission intensity exhibits a clear transition from the linear to the superlinear regime. The

relationship between the output lasing intensity versus the pump energy results in a typical “S-shaped” characteristic curve in the log-log scale (the inset in Figure 4c), which confirms the observed emission belonging to the incoherent random lasing rather than ASE phenomenon.<sup>28,32,67</sup> It can be generally explained by the well-known diffusion model with the gain, which excludes the optical interference effects.<sup>29</sup> In fact, such similar observation of the incoherent RL without coherent feedbacks has been previously reported by many authors from the solution-processed MAPbBr<sub>3</sub> perovskite thin films.<sup>28,30,67,68</sup>

To understand the effect of grain boundary coalescence and the defect passivation on the lasing performance of thin films, we measured the pump energy-dependent PL spectra for all the laser-treated samples as well (see Figure S13). The output lasing intensities of the laser-treated samples were found substantially higher than that of the bare sample. Both the extracted line widths and integrated intensities of the output spectral emission are plotted in Figure 4a,b, wherein the two parameter values have a clear transition at the lasing threshold point. Noticeably, the measurement of the lasing threshold value for the as-treated samples was much lower than that of the bare sample. Among all the laser-treated samples, the sample treated at  $F_{\text{treat}} = 10 \text{ mJ}/\text{cm}^2$  exhibits a giant reduction in the RL threshold compared to that of bare sample (Figure 4c), that is from  $F_{\text{pump}} = 11.54$  to  $0.92 \mu\text{J}/\text{cm}^2$ . To the best of our knowledge, this lasing threshold is significantly lower than the previous reports in the relevant field (see Table S3).

In addition, the linear growth of the output laser intensity with respect to the pump energy fluence is characterized for the situations above the lasing threshold, which is defined as a slope efficiency ( $\eta$ ) of the optical pumping. As shown in Figure 4c, the measurement of  $\eta$  seems to improve notably for the perovskite samples treated by the femtosecond laser irradiation, and it exhibits a champion performance at the

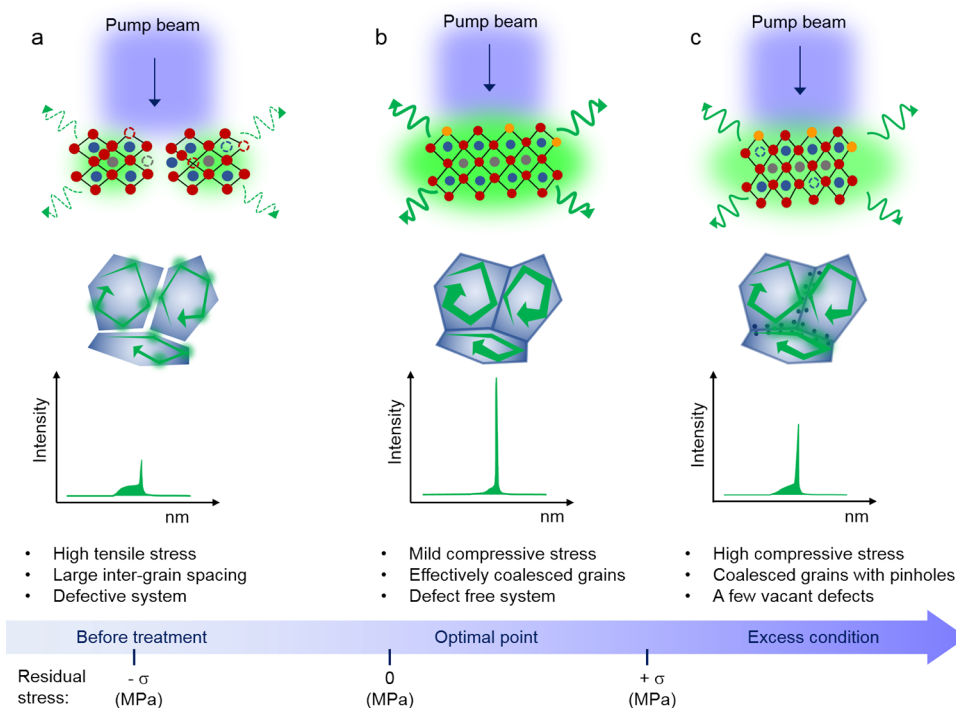


**Figure 5.** Concept model: PL and RL behaviors of MAPbBr<sub>3</sub> perovskite thin films upon the femtosecond laser-induced modification of the crystal structures and grain boundary coalescence. (a–c) Top: arrangement of perovskite crystal structures with their residual strain, defect structures, and corresponding PL behavior, in which the solid dots represent the atoms and molecules (red: Br, blue: Pb, ash: MA, and yellow: O<sub>2</sub>) and hollow dots for the corresponding vacancy defects. Middle: distribution of perovskite grains and in-plane optical scattering loops in them, the circular glows at the grain boundaries, and pinholes (small blue dots) indicate the out-of-plane scattering losses. After the femtosecond laser treatment, the grain boundaries of the perovskite sample effectively coalesce together. Bottom: the intensities of the RL emission from the samples. The perfect adjacent grain coalescence and intense lasing emission (such as presented in this work) are obtained with the mild compressive stress condition as exhibited in panel b.

laser treatment fluence of  $F_{\text{treat}} = 10 \text{ mJ/cm}^2$ , with a large value of  $\eta \sim 2398$ , almost 15 times more increment than that of the bare sample ( $\eta \sim 150$ ). However, for the higher fluence of laser treatments, the measured  $\eta$  values are seen to slightly decrease, which might be due to the large crystalline deformation and generation of V(Pb) defects by the excessive compressive stress (as discussed with DFT calculation results).

Additionally, the direct measurements of the material gain and all-optical loss of the samples will provide detailed insights into the gain-loss balance before and after the laser treatment (see supplementary section 4 for more experimental details). As discussed above, the number of scattering events and the mean free path length must be very large to achieve sufficient optical gain for overcoming the overall optical losses inside the active medium, thus leading to the highly intense RL output through light amplification.

By using a variable stripe length (VSL) method, we quantitatively determined the gain values of our samples. The RL emission intensity,  $I(\lambda)$ , transmitting through one end of the pump light stripe, is directly related to the gain coefficient of the sample by the following equation:<sup>69</sup>

$$I(\lambda) = \frac{AI_0}{g(\lambda)} (e^{g(\lambda)L} - 1) \quad (3)$$

where  $L$  is the stripe length of the incident pump light beam on the sample surface, and  $A$  is the cross-section constant;  $I_0$  is the pumping light intensity, and  $g(\lambda)$  is the net gain coefficient of the material. The dependence of  $I(\lambda)$  on the  $L$  parameter was calculated by applying eq 3 at the small-signal regime; thus, a

series of optical gain values can be obtained for the samples before and after the femtosecond laser treatments (known as Shaklee and Leheny's method, shown in Figure 4d).

In this study, we are quantifying the combined effect of the out-of-plane scattering losses and the material self-absorption loss with the overall optical loss coefficient of the thin films. Therefore, the net loss inside the active medium is eventually considered a determined factor of the threshold and overall efficiency of the laser device. The net loss experienced when the light follows the Beer–Lambert law  $I(\lambda) = I_0 e^{-\alpha z}$ , where  $z$  is the distance from the edge of the perovskite film to the nearest end of the pump light stripe and  $\alpha$  is the loss coefficient. The measured data of the output intensity with variable distances from the edge of the sample were then fitted with the Beer–Lambert law for extracting the loss coefficient values (shown in Figure 4e).

Figure 4f shows the optical gain and loss coefficients of the samples before and after the femtosecond laser treatments. It is seen that the obtained net gain coefficient for the laser-treated sample is higher than the bare one. For example, in the case of  $F_{\text{treat}} = 10 \text{ mJ/cm}^2$ , the obtained optimal gain coefficient of  $g = 63.23 \text{ cm}^{-1}$  shows an increment of more than 43.0% compared with the bare sample ( $g = 44.15 \text{ cm}^{-1}$ ). At the same time, the net optical loss coefficient associated with the laser-treated sample at  $F_{\text{treat}} = 10 \text{ mJ/cm}^2$  is decreased to a minimum value ( $\alpha = 5.08 \text{ cm}^{-1}$ ) when compared with other samples. This is a key factor in why, despite the surface treated with  $F_{\text{treat}} = 20 \text{ mJ/cm}^2$  having a higher PL yield, the sample with  $F_{\text{treat}} = 10 \text{ mJ/cm}^2$  has the lowest lasing threshold of all the others. Such an improvement in the optical gain and loss coefficient of the



sample is mainly attributed to two reasons: (i) reducing the nonradiative deep defect density along the grain boundaries, (ii) increasing the in-plane scattering effect/light confinement in the thin film by suppressing the out-of-plane scattering losses through the wide intergrain spacings.

We tried to understand how the nonthermal and thermal effects induced by the femtosecond laser pulses are influencing the RL performance of the perovskite thin film; the key elements in this study can be compiled as follows: (i) most of the spin-coated perovskite thin films contain the wide intergrain spacing and severe cracks due to the thermally induced residual tensile strain and their highly brittle nature. This consequently increases the out-of-plane scattering losses while used as a light confining medium. Besides, the higher density of deep defects along the grain boundaries offers fast nonradiative decay channels to the excited carriers, thus preventing the carriers from populating at the excited states. Eventually, these factors severely hinder the development of a high-performance laser device (Figure 5a). (ii) By optimally regulating the femtosecond laser-induced thermal and non-thermal effects, we can effectively coalesce the adjacent grain boundaries and reduce the nonradiative deep defects associated with the MAPbBr<sub>3</sub> polycrystalline thin films. The optimal grain boundary coalescence effect increases the in-plane optical loops or light confinement in the thin films for achieving a higher gain coefficient (Figure 5b). The DFT calculation results show that the mild compressive stress condition (0 MPa <  $\sigma$  < -15 MPa) developed in the thin films can considerably increase the  $E_{\text{form}}$  and inhibit the defect density. Eventually, the PL and RL performance of the femtosecond laser-treated sample can be significantly enhanced. (iii) When the laser treatment fluence continues to increase, the high compressive stress can lead to the development of new vacant defects and an array of pinholes at the grain boundaries, which slightly decreases the output lasing intensity by decreasing the radiative recombination and increasing the out-of-plane scattering losses, respectively (Figure 5c).

## CONCLUSIONS

In this study, we have demonstrated an effective method to manipulate the crystalline properties of the MAPbBr<sub>3</sub> perovskite thin films by regulating the magnitudes of the nonthermal and thermal effects during the femtosecond laser treatment. Through adjusting the laser fluence, we have tuned the above two effects and evidently eliminated the wide intergrain gaps with the reduced number of pinholes. The experimental results along with the DFT calculations unveil that the mild compressive stress condition (0 MPa <  $\sigma$  < -15 MPa) induced by the optimum nonthermal effect can effectively increase the formation energy of various defects to inhibit the overall density of defects. As a result, the measurement of PL lifetime is prolonged by about 371.35% and the PL intensity is enhanced about 31 times. A comprehensive gain coefficient analysis using the VSL method confirms that this femtosecond laser treatment strategy can enhance the optical gain coefficient to overcome the all-optical loss coefficient. Eventually, the measurement of RL threshold was greatly reduced from 11.54 to 0.92  $\mu\text{J}/\text{cm}^2$ , and the slope efficiency was increased more than 15 times. This study provides a promising novel method for fabricating high-performance thin-film laser devices, light-emitting diodes, and other luminescence devices for various optoelectronic applications.

## ASSOCIATED CONTENT

### Supporting Information

The Supporting Information is available free of charge at <https://pubs.acs.org/doi/10.1021/acsphotonics.3c00669>.

Materials and methods, schematic of the optical setup employed for the femtosecond laser treatment, SEM images of MAPbBr<sub>3</sub> samples after laser treatment, GIXRD and  $\mu$ -XRD analysis of femtosecond laser treatment samples, short and long life-time components measured through TRPL plots, measured RL spectra of laser-treated samples, the state-of-the-art of random laser threshold values, and experimental details and background theory for optical gain and loss coefficient measurements (PDF)

## AUTHOR INFORMATION

### Corresponding Authors

**Zhiming Shi** – State Key Laboratory of Luminescence and Applications, Changchun Institute of Optics, Fine Mechanics and Physics, Chinese Academy of Sciences, Changchun 130033, P.R. China; University of Chinese Academy of Sciences, Beijing 100049, P. R. China; [orcid.org/0000-0002-1207-570X](https://orcid.org/0000-0002-1207-570X); Email: [shizm@ciomp.ac.cn](mailto:shizm@ciomp.ac.cn)

**Weili Yu** – GPL Photonic Laboratory, State Key Laboratory of Luminescence and Applications, Changchun Institute of Optics, Fine Mechanics and Physics, Chinese Academy of Sciences, Changchun 130033, P.R. China; University of Chinese Academy of Sciences, Beijing 100049, P. R. China; Email: [weili.yu@ciomp.ac.cn](mailto:weili.yu@ciomp.ac.cn)

**Jianjun Yang** – GPL Photonic Laboratory, State Key Laboratory of Luminescence and Applications, Changchun Institute of Optics, Fine Mechanics and Physics, Chinese Academy of Sciences, Changchun 130033, P.R. China; Center of Materials Science and Optoelectronics Engineering, University of Chinese Academy of Sciences, Beijing 100049, China; University of Chinese Academy of Sciences, Beijing 100049, P. R. China; [orcid.org/0000-0002-6703-4403](https://orcid.org/0000-0002-6703-4403); Email: [jjyang@ciomp.ac.cn](mailto:jjyang@ciomp.ac.cn)

### Authors

**Rahul A. Rajan** – GPL Photonic Laboratory, State Key Laboratory of Luminescence and Applications, Changchun Institute of Optics, Fine Mechanics and Physics, Chinese Academy of Sciences, Changchun 130033, P.R. China; University of Chinese Academy of Sciences, Beijing 100049, P. R. China

**Xiaobao Ma** – State Key Laboratory of Luminescence and Applications, Changchun Institute of Optics, Fine Mechanics and Physics, Chinese Academy of Sciences, Changchun 130033, P.R. China; University of Chinese Academy of Sciences, Beijing 100049, P. R. China

**Dabing Li** – State Key Laboratory of Luminescence and Applications, Changchun Institute of Optics, Fine Mechanics and Physics, Chinese Academy of Sciences, Changchun 130033, P.R. China; University of Chinese Academy of Sciences, Beijing 100049, P. R. China

Complete contact information is available at:

<https://pubs.acs.org/doi/10.1021/acsphotonics.3c00669>

### Author Contributions

R.A.R., W.Y., and J.Y. conceived the study. R.A.R. performed experiments and analyze the results. X.M. and Z.S. performed

the DFT calculations. J.Y. and W.Y. supervise the overall work. All the authors discussed the results and commented on the manuscript.

### Funding

This work was supported by the National Natural Science Foundation of China (Grant Nos. 91750205, 11674178), Jilin Provincial Science & Technology Development Project (Grant No. 20200201086JC). R.A.R. gratefully acknowledges his support from UCAS Full-Fellowship for International Students (20190442).

### Notes

The authors declare the following competing financial interest(s): R.A.R., W.Y., and J.Y. are inventors on the patent application with the patent application number: 202211426423.0, application date: 2022.11.15. The other authors declare that they have no competing interests. R.A.R., W.Y., and J.Y. are inventors on the patent application with the patent application number: 202211426423.0, the application date: 2022.11.15. The other authors declare that they have no competing interests.

## ACKNOWLEDGMENTS

We thank Dr. Wenchi Kong for the preparation of experimental samples and Mr. Yucai Lin for measuring the UV–vis absorption spectra.

## REFERENCES

- (1) Sutherland, B. R.; Sargent, E. H. Perovskite Photonic Sources. *Nat. Photonics* **2016**, *10*, 295–302.
- (2) Hill, M. T.; Gather, M. C. Advances in Small Lasers. *Nat. Photonics* **2014**, *8*, 908–918.
- (3) Hasegawa, S.; Fujimoto, M.; Atsumi, T.; Hayasaki, Y. In-Process Monitoring in Laser Grooving with Line-Shaped Femtosecond Pulses Using Optical Coherence Tomography. *Light: Adv. Manuf.* **2022**, *3*, 427–436.
- (4) Flamini, F.; Magrini, L.; Rab, A. S.; Spagnolo, N.; D'Ambrosio, V.; Mataloni, P.; Sciarino, F.; Zandrini, T.; Crespi, A.; Ramponi, R.; Osellame, R. Thermally Reconfigurable Quantum Photonic Circuits at Telecom Wavelength by Femtosecond Laser Micromachining. *Light: Sci. Appl.* **2015**, *4*, No. e354.
- (5) Colella, S.; Mazzeo, M.; Rizzo, A.; Gigli, G.; Listorti, A. The Bright Side of Perovskites. *J. Phys. Chem. Lett.* **2016**, *7*, 4322–4334.
- (6) Sun, K.; Tan, D.; Fang, X.; Xia, X.; Lin, D.; Song, J.; Lin, Y.; Liu, Z.; Gu, M.; Yue, Y.; Qiu, J. Three-Dimensional Direct Lithography of Stable Perovskite Nanocrystals in Glass. *Science* **2022**, *375*, 307–310.
- (7) Lee, S. J.; Cheng, H. C.; Wang, Y.; Zhou, B.; Li, D.; Wang, G.; Liu, Y.; Guo, J.; Wu, H.; Kang, D. J.; Huang, Y.; Duan, X. Lead Halide Perovskite Sensitized WSe<sub>2</sub> Photodiodes with Ultrahigh Open Circuit Voltages. *eLight* **2023**, *3*, 1–10.
- (8) Dong, H.; Ran, C.; Gao, W.; Li, M.; Xia, Y.; Huang, W. Metal Halide Perovskite for next-Generation Optoelectronics: Progresses and Prospects. *eLight* **2023**, *3*, 1–16.
- (9) Liu, Y.; Ji, Z.; Cen, G.; Sun, H.; Wang, H.; Zhao, C.; Wang, Z. L.; Mai, W. Perovskite-Based Color Camera Inspired by Human Visual Cells. *Light: Sci. Appl.* **2023**, *12*, 43.
- (10) Ju, S.; Zhu, Y.; Hu, H.; Liu, Y.; Xu, Z.; Zheng, J.; Mao, C.; Yu, Y.; Yang, K.; Lin, L.; Guo, T.; Li, F. Dual-Function Perovskite Light-Emitting/Sensing Devices for Optical Interactive Display. *Light: Sci. Appl.* **2022**, *11*, 331.
- (11) Toulouse, A.; Drozella, J.; Thiele, S.; Giessen, H.; Herkommer, A. 3D-Printed Miniature Spectrometer for the Visible Range with a 100 × 100 Mm<sup>2</sup> Footprint. *Light: Adv. Manuf.* **2021**, *2*, 20–30.
- (12) Saidaminov, M. I.; Abdelhady, A. L.; Murali, B.; Alarousu, E.; Burlakov, V. M.; Peng, W.; Dursun, I.; Wang, L.; He, Y.; Maculan, G.; Goriely, A.; Wu, T.; Mohammed, O. F.; Bakr, O. M. High-Quality Bulk Hybrid Perovskite Single Crystals within Minutes by Inverse Temperature Crystallization. *Nat. Commun.* **2015**, *6*, 1–6.
- (13) Shi, D.; Adinolfi, V.; Comin, R.; Yuan, M.; Alarousu, E.; Buin, A.; Chen, Y.; Hoogland, S.; Rothenberger, A.; Katsiev, K.; Losovsky, Y.; Zhang, X.; Dowben, P. A.; Mohammed, O. F.; Sargent, E. H.; Bakr, O. M. Low Trap-State Density and Long Carrier Diffusion in Organolead Trihalide Perovskite Single Crystals. *Science* **2015**, *347*, 519–522.
- (14) Wang, J. X.; Wang, X.; Yin, J.; Gutiérrez-Arzaluz, L.; He, T.; Chen, C.; Han, Y.; Zhang, Y.; Bakr, O. M.; Eddaoudi, M.; Mohammed, O. F. Perovskite-Nanosheet Sensitizer for Highly Efficient Organic X-Ray Imaging Scintillator. *ACS Energy Lett.* **2022**, *7*, 10–16.
- (15) Poh, E. T.; Lim, S. X.; Sow, C. H. Multifaceted Approaches to Engineer Fluorescence in Nanomaterials via a Focused Laser Beam. *Light: Adv. Manuf.* **2022**, *3*, 85–104.
- (16) Huang, P.; Sun, S.; Lei, H.; Zhang, Y.; Qin, H.; Zhong, H. Nonlocal Interaction Enhanced Biexciton Emission in Large CsPbBr<sub>3</sub> Nanocrystals. *eLight* **2023**, *3*, 10.
- (17) Sun, X.; Zhang, Y.; Ge, W. Photo-Induced Macro/Mesoscopic Scale Ion Displacement in Mixed-Halide Perovskites: Ring Structures and Ionic Plasma Oscillations. *Light: Sci. Appl.* **2022**, *11*, 262.
- (18) Wang, H.; Xu, W.; Wei, Q.; Peng, S.; Shang, Y.; Jiang, X.; Yu, D.; Wang, K.; Pu, R.; Zhao, C.; Zang, Z.; Li, H.; Zhang, Y.; Pan, T.; Peng, Z.; Shen, X.; Ling, S.; Liu, W.; Gao, F.; Ning, Z. In-Situ Growth of Low-Dimensional Perovskite-Based Insular Nanocrystals for Highly Efficient Light Emitting Diodes. *Light: Sci. Appl.* **2023**, *12*, 62.
- (19) Yang, H.; Chen, X.; Chu, Y.; Sun, C.; Lu, H.; Yuan, M.; Zhang, Y.; Long, G.; Zhang, L.; Li, X. A Universal Hydrochloric Acid-Assistant Powder-to-Powder Strategy for Quick and Mass Preparation of Lead-Free Perovskite Microcrystals. *Light: Sci. Appl.* **2023**, *12*, 75.
- (20) Murali, B.; Kolli, H. K.; Yin, J.; Ketavath, R.; Bakr, O. M.; Mohammed, O. F. Single Crystals: The Next Big Wave Of Perovskite Optoelectronics. **2020**, *2*, 184–214.
- (21) Zhou, Z.; Ou, X.; Fang, Y.; Alkharaji, E.; Xu, R.; Wan, Y.; Bowers, J. E. Prospects and Applications of on-Chip Lasers. *eLight* **2023**, *3*, 1–25.
- (22) Gao, L.; Zhang, Y.; Gou, L.; Wang, Q.; Wang, M.; Zheng, W.; Wang, Y.; Yip, H. L.; Zhang, J. High Efficiency Pure Blue Perovskite Quantum Dot Light-Emitting Diodes Based on Formamidinium Manipulating Carrier Dynamics and Electron State Filling. *Light: Sci. Appl.* **2022**, *11*, 346.
- (23) Li, H.; Wang, Y.; Gao, H.; Zhang, M.; Lin, R.; Wu, P.; Xiao, K.; Tan, H. Revealing the Output Power Potential of Bifacial Monolithic All-Perovskite Tandem Solar Cells. *eLight* **2022**, *2*, 21.
- (24) Yu, H.; Ding, H.; Zhang, Q.; Gu, Z.; Gu, M. Three-Dimensional Direct Laser Writing of PEGda Hydrogel Microstructures with Low Threshold Power Using a Green Laser Beam. *Light: Adv. Manuf.* **2021**, *2*, 31–38.
- (25) Zhang, D.; Fu, Y.; Zhan, H.; Zhao, C.; Gao, X.; Qin, C.; Wang, L. Suppressing Thermal Quenching via Defect Passivation for Efficient Quasi-2D Perovskite Light-Emitting Diodes. *Light: Sci. Appl.* **2022**, *11*, 69.
- (26) Xing, G.; Mathews, N.; Lim, S. S.; Yantara, N.; Liu, X.; Sabba, D.; Grätzel, M.; Mhaisalkar, S.; Sum, T. C. Low-Temperature Solution-Processed Wavelength-Tunable Perovskites for Lasing. *Nat. Mater.* **2014**, *13*, 476–480.
- (27) Zhong, H.; Yu, Y.; Zheng, Z.; Ding, Z.; Zhao, X.; Yang, J.; Wei, Y.; Chen, Y.; Yu, S. Ultra-Low Threshold Continuous-Wave Quantum Dot Mini-BIC Lasers. *Light: Sci. Appl.* **2023**, *12*, 100.
- (28) Weng, G.; Xue, J.; Tian, J.; Hu, X.; Bao, X.; Lin, H.; Chen, S.; Zhu, Z.; Chu, J. Picosecond Random Lasing Based on Three-Photon Absorption in Organometallic Halide CH<sub>3</sub>NH<sub>3</sub>PbBr<sub>3</sub> Perovskite Thin Films. *ACS Photonics* **2018**, *5*, 2951–2959.
- (29) Wiersma, D. S. The Physics and Applications of Random Lasers. *Nat. Phys.* **2008**, *4*, 359–367.
- (30) Kao, T. S.; Chou, Y. H.; Chou, C. H.; Chen, F. C.; Lu, T. C. Lasing Behaviors upon Phase Transition in Solution-Processed Perovskite Thin Films. *Appl. Phys. Lett.* **2014**, *105*, 231108.

- (31) De Giorgi, M. L.; Krieg, F.; Kovalenko, M. V.; Anni, M. Amplified Spontaneous Emission Threshold Reduction and Operational Stability Improvement in CsPbBr<sub>3</sub> Nanocrystals Films by Hydrophobic Functionalization of the Substrate. *Sci. Rep.* **2019**, *9*, 17964.
- (32) Weng, G.; Tian, J.; Chen, S.; Xue, J.; Yan, J.; Hu, X.; Chen, S.; Zhu, Z.; Chu, J. Giant Reduction of the Random Lasing Threshold in CH<sub>3</sub>NH<sub>3</sub>PbBr<sub>3</sub> Perovskite Thin Films by Using a Patterned Sapphire Substrate. *Nanoscale* **2019**, *11*, 10636–10645.
- (33) Wang, Y.-C.; Li, H.; Hong, Y.-H.; Hong, K. B.; Chen, F.-C.; Hsu, C.-H.; Lee, R.-K.; Conti, C.; Kao, T. S.; Lu, T.-C. Flexible Organometal-Halide Perovskite Lasers for Speckle Reduction in Imaging Projection. *ACS Nano* **2019**, *13*, 5421–5429.
- (34) Hong, Y. H.; Kao, T. S. Room-Temperature Random Lasing of Metal-Halide Perovskites: Via Morphology-Controlled Synthesis. *Nanoscale Adv.* **2020**, *2*, 5833–5840.
- (35) Kao, T. S.; Chou, Y.-H.; Hong, K. B.; Huang, J.-F.; Chou, C.-H.; Kuo, H.-C.; Chen, F.-C.; Lu, T.-C. Controllable Lasing Performance in Solution-Processed Organic-Inorganic Hybrid Perovskites. *Nanoscale* **2016**, *8*, 18483–18488.
- (36) Kim, H. S.; Park, N. G. Importance of Tailoring Lattice Strain in Halide Perovskite Crystals. *NPG Asia Mater.* **2020**, *12*, 78.
- (37) An, Q.; Paulus, F.; Becker-Koch, D.; Cho, C.; Sun, Q.; Weu, A.; Bitton, S.; Tessler, N.; Vaynzof, Y. Small Grains as Recombination Hot Spots in Perovskite Solar Cells. *Matter* **2021**, *4*, 1683–1701.
- (38) Sundaram, S. K.; Mazur, E. Inducing and Probing Non-Thermal Transitions in Semiconductors Using Femtosecond Laser Pulses. *Nat. Mater.* **2002**, *1*, 217–224.
- (39) Siegal, Y.; Glezer, E. N.; Huang, L.; Mazur, E. Laser-Induced Phase Transitions in Semiconductors. *Annu. Rev. Mater. Sci.* **1995**, *25*, 223–247.
- (40) Stampfli, P.; Bennemann, K. H. Dynamical Theory of the Laser-Induced Lattice Instability of Silicon. *Phys. Rev. B* **1992**, *46*, 10686–10692.
- (41) Falkovsky, L. A.; Mishchenko, E. G. Electron-Lattice Kinetics of Metals Heated by Ultrashort Laser Pulses. *J. Exp. Theor. Phys.* **1999**, *88*, 84–88.
- (42) Chen, J. K.; Beraun, J. E.; Tzou, D. Y. Thermomechanical Response of Metals Heated by Ultrashort-Pulsed Lasers. *J. Therm. Stresses* **2002**, *25*, 539–558.
- (43) Naghilou, A.; He, M.; Schubert, J. S.; Zhigilei, L. V.; Kautek, W. Femtosecond Laser Generation of Microbumps and Nanojets on Single and Bilayer Cu/Ag Thin Films. *Phys. Chem. Chem. Phys.* **2019**, *21*, 11846–11860.
- (44) Yang, J.; Zhao, Y.; Zhang, N.; Liang, Y.; Wang, M. Ablation of Metallic Targets by High-Intensity Ultrashort Laser Pulses. *Phys. Rev. B* **2007**, *76*, 1–10.
- (45) Khalkhali, M.; Rajabpour, A.; Khoeini, F. Thermal Transport across Grain Boundaries in Polycrystalline Silicene: A Multiscale Modeling. *Sci. Rep.* **2019**, *9*, 1–12.
- (46) Amer, M. S.; El-Ashry, M. A.; Dosser, L. R.; Hix, K. E.; Maguire, J. F.; Irwin, B. Femtosecond versus Nanosecond Laser Machining: Comparison of Induced Stresses and Structural Changes in Silicon Wafers. *Appl. Surf. Sci.* **2005**, *242*, 162–167.
- (47) Morales, J.; Petkova, G.; Cruz, M.; Caballero, A. Nanostructured Lead Dioxide Thin Electrode. *Electrochem. Solid-State Lett.* **2004**, *7*, A75–A77.
- (48) Juarez-perez, E. J.; Ono, L. K.; Maeda, M.; Jiang, Y.; Hawash, Z.; Qi, Y. Photodecomposition and Thermal Decomposition in Methylammonium Halide Lead Perovskites and Inferred Design Principles to Increase Photovoltaic Device Stability. *J. Mater. Chem. A* **2018**, *6*, 9604–9612.
- (49) De Giorgi, M. L.; Lippolis, T.; Jamaludin, N. F.; Soci, C.; Bruno, A.; Anni, M. Origin of Amplified Spontaneous Emission Degradation in MAPbBr<sub>3</sub> Thin Films under Nanosecond-UV Laser Irradiation. *J. Phys. Chem. C* **2020**, *124*, 10696–10704.
- (50) Godding, J. S. W.; Ramadan, A. J.; Lin, Y. H.; Schutt, K.; Snaith, H. J.; Wenger, B. Oxidative Passivation of Metal Halide Perovskites. *Joule* **2019**, *3*, 2716–2731.
- (51) Prevey, P. S. X-Ray Diffraction Residual Stress Techniques. *Mater. Charact.* **1986**, *10*, 380–392.
- (52) Delbergue, D.; Texier, D.; Levesque, M.; Bocher, P.; Delbergue, D.; Texier, D.; Levesque, M.; Comparison, P. B.; Stress, X. R. Comparison of Two X-Ray Residual Stress Measurement Methods: Sin<sup>2</sup>  $\psi$  and Cos  $\alpha$ , Through the Determination of a Martensitic Steel X-Ray Elastic Constant. *Residual Stresses* **2016**, *2*, 55–60.
- (53) Zarabina, N.; Rasuli, R. Electronic and Optical Properties of Halide Double-Perovskites under Strain: A Density Functional Study. *Energy Sources, Part A* **2021**, *43*, 2443–2455.
- (54) Ran, C.; Xu, J.; Gao, W.; Huang, C.; Dou, S. Defects in Metal Triiodide Perovskite Materials towards High-Performance Solar Cells: Origin, Impact, Characterization, and Engineering. *Chem. Soc. Rev.* **2018**, *47*, 4581–4610.
- (55) Boopathi, K. M.; Martín-García, B.; Ray, A.; Pina, J. M.; Marras, S.; Saidaminov, M. I.; Bonaccorso, F.; Di Stasio, F.; Sargent, E. H.; Manna, L.; Abdelhady, A. L. Permanent Lattice Compression of Lead-Halide Perovskite for Persistently Enhanced Optoelectronic Properties. *ACS Energy Lett.* **2020**, *5*, 642–649.
- (56) Lei, L.; Dong, Q.; Gundogdu, K.; So, F. Metal Halide Perovskites for Laser Applications. *Adv. Funct. Mater.* **2021**, *31*, 1–21.
- (57) Leyden, M. R.; Matsushima, T.; Bencheikh, F.; Adachi, C. Film Transfer of Structured Organo-Lead-Halide Perovskite for Low-Cost Lasing Applications. *Appl. Phys. Lett.* **2019**, *115*, 141106.
- (58) Liu, Y.; Lu, H.; Niu, J.; Zhang, H.; Lou, S.; Gao, C.; Zhan, Y.; Zhang, X.; Jin, Q.; Zheng, L. Temperature-Dependent Photoluminescence Spectra and Decay Dynamics of MAPbBr<sub>3</sub> and MAPbI<sub>3</sub> Thin Films. *AIP Adv.* **2018**, *8*, No. 095108.
- (59) Xing, J.; Zhao, C.; Zou, Y.; Kong, W.; Yu, Z.; Shan, Y.; Dong, Q.; Zhou, D.; Yu, W.; Guo, C. Modulating the Optical and Electrical Properties of MAPbBr<sub>3</sub> Single Crystals via Voltage Regulation Engineering and Application in Memristors. *Light: Sci. Appl.* **2020**, *9*, 111.
- (60) Fang, X.; Zhang, K.; Li, Y.; Yao, L.; Zhang, Y.; Wang, Y.; Zhai, W.; Tao, L.; Du, H.; Ran, G. Effect of Excess PbBr<sub>2</sub> on Photoluminescence Spectra of CH<sub>3</sub>NH<sub>3</sub>PbBr<sub>3</sub> Perovskite Particles at Room Temperature. *Appl. Phys. Lett.* **2016**, *108*, No. 071109.
- (61) Van De Riet, I.; Fang, H.-H.; Adjokate, S.; Kahmann, S.; Loi, M. A. Influence of Morphology on Photoluminescence Properties of Methylammonium Lead Tribromide Films. *J. Lumin.* **2020**, *220*, No. 117033.
- (62) Sun, S.; Yuan, D.; Xu, Y.; Wang, A.; Deng, Z. Ligand-Mediated Synthesis of Shape-Controlled Cesium Lead Halide Perovskite Nanocrystals via Reprecipitation Process at Room Temperature. *ACS Nano* **2016**, *10*, 3648–3657.
- (63) Yantara, N.; Bhaumik, S.; Yan, F.; Sabba, D.; Dewi, H. A.; Mathews, N.; Boix, P. P.; Demir, H. V.; Mhaisalkar, S. Inorganic Halide Perovskites for Efficient Light-Emitting Diodes. *J. Phys. Chem. Lett.* **2015**, *6*, 4360–4364.
- (64) Moloney, E. G.; Yeddu, V.; Saidaminov, M. I. Strain Engineering in Halide Perovskites. *ACS Mater. Lett.* **2020**, *2*, 1495–1508.
- (65) Uhd Jepsen, P.; Schairer, W.; Libon, I. H.; Lemmer, U.; Hecker, N. E.; Birkholz, M.; Lips, K.; Schall, M. Ultrafast Carrier Trapping in Microcrystalline Silicon Observed in Optical Pump-Terahertz Probe Measurements. *Appl. Phys. Lett.* **2001**, *79*, 1291–1293.
- (66) Xing, G.; Xing, G.; Li, M.; Sie, E. J.; Wang, D.; Sulistio, A.; Ye, Q. L.; Huan, C. H. A.; Wu, T.; Sum, T. C. Charge Transfer Dynamics in Cu-Doped ZnO Nanowires. *Appl. Phys. Lett.* **2011**, *98*, 2011–2014.
- (67) Mallick, S. P.; Hong, Y. H.; Chen, L. R.; Kao, T. S.; Lu, T. C. Effect of Passivation Layer on the Thin Film Perovskite Random Lasers. *Materials* **2020**, *13*, 2322.
- (68) Zhang, X.; Yan, S.; Tong, J.; Shi, X.; Zhang, S.; Chen, C.; Xiao, Y. Y.; Han, C.; Zhai, T. Perovskite Random Lasers on Fiber Facet. *NANO* **2020**, *9*, 935–941.
- (69) Shaklee, K. L.; Leheny, R. F. Direct Determination of Optical Gain in Semiconductor Crystals. *Appl. Phys. Lett.* **1971**, *18*, 475–477.